APL Materials

Crossover between distinct symmetries in solid solutions of rare earth nickelates

Cite as: APL Mater. **9**, 081119 (2021); https://doi.org/10.1063/5.0057216
Submitted: 18 May 2021 . Accepted: 14 July 2021 . Published Online: 30 August 2021

Jennifer Fowlie, Bernat Mundet, Constance Toulouse, Alexander Schober, Mael Guennou, Claribel Domínguez, Marta Gibert, Duncan T. L. Alexander, Jens Kreisel, and Jean-Marc Triscone

COLLECTIONS

F This paper was selected as Featured

SCI This paper was selected as Scilight

AIP Publishing

APL Materials ARTICLE scitation.org/journal/apm

Crossover between distinct symmetries in solid solutions of rare earth nickelates

Cite as: APL Mater. 9, 081119 (2021); doi: 10.1063/5.0057216
Submitted: 18 May 2021 • Accepted: 14 July 2021 •
Published Online: 30 August 2021

Jennifer Fowlie,[1,a)] **Bernat Mundet,**[1,2] **Constance Toulouse,**[3,4] **Alexander Schober,**[3] **Mael Guennou,**[3,4] **Claribel Domínguez,**[1] **Marta Gibert,**[5] **Duncan T. L. Alexander,**[2] **Jens Kreisel,**[4] **and Jean-Marc Triscone**[1]

AFFILIATIONS

[1] DQMP–University of Geneva, École de Physique, 24, Quai Ernest-Ansermet, CH-1211 Geneva, Switzerland
[2] Electron Spectrometry and Microscopy Laboratory (LSME), Institute of Physics (IPHYS), École Polytechnique Fédérale de Lausanne (EPFL), 1015 Lausanne, Switzerland
[3] Materials Research and Technology Department, Luxembourg Institute of Science and Technology, 41 rue du Brill, L-4422 Belvaux, Luxembourg
[4] Department of Physics and Materials Science, University of Luxembourg, 41 rue du Brill, L-4422 Belvaux, Luxembourg
[5] Physik-Institut, University of Zurich, Winterthurerstrasse 190, Zurich, Switzerland

[a)] **Author to whom correspondence should be addressed:** jennifer.fowlie@unige.ch

ABSTRACT

A strong coupling of the lattice to functional properties is observed in many transition metal oxide systems, such as the ABO_3 perovskites. In the quest for tailor-made materials, it is essential to be able to control the structural properties of the compound(s) of interest. Here, thin film solid solutions that combine $NdNiO_3$ and $LaNiO_3$, two materials with the perovskite structure but distinct space groups, are analyzed. Raman spectroscopy and scanning transmission electron microscopy are combined in a synergistic approach to fully determine the mechanism of the structural crossover with chemical composition. It is found that the symmetry transition is achieved by phase coexistence in a way that depends on the substrate selected. These results carry implications for analog-tuning of physical properties in future functional materials based on these compounds.

I. INTRODUCTION

Perovskite oxides with the general formula ABO_3 comprise a large family of materials owing to the wide variety of cations that can be substituted onto the A- and B-sites. This high degree of flexibility in chemistry is reflected in the plethora of physical properties that can be obtained ranging from superconductivity to ferroelectricity.[1,2]

Part of the reason for the chemical flexibility of the perovskite oxide structure stems from the multiple stable ABO_3 space groups. The ABO_3 lattice is comprised of corner-sharing BO_6 octahedra. A total of 15 space groups can be derived through only cooperative tilts and rotations of the octahedra while maintaining their shape.[3,4] Cation substitution, polar and antipolar ionic displacements, or Jahn–Teller effects can also be accommodated in distorted perovskite structures, giving rise to a great variety of crystal symmetries and corresponding physical properties.[5–7]

Even subtle structural effects can generate rich phase diagrams due to the delicate tuning of, for instance, the B–O–B orbital overlap or the magnetic exchange angle. One such phase diagram is that of the rare earth nickelates ($RNiO_3$, where R = a rare earth cation), where all except $LaNiO_3$ are insulating and antiferromagnetic at low temperature. This ground state is characterized by a charge and bond disproportionation.[8] Importantly, the temperatures up to which the insulating and antiferromagnetic states are stabilized strongly depend on the Ni–O–Ni bond angle.[9] As the rare earth cation is varied from Lu to Pr, the temperature of the insulator-to-metal transition in bulk samples is decreased from around 600 K to less than 100 K.[10] This extraordinary change is brought about through a reduction in the BO_6 tilts and, therefore, a straightening of the Ni–O–Ni bond angle. This tuning is not continuous, however, as there are only a finite number of rare earth elements that can be substituted onto the A-site. In order to achieve quasi-analog control of the various phases, another parameter must be tuned.[11,12] This could be an external parameter, such as pressure,[13] but this is experimentally challenging and of limited practical relevance for implementation in future devices. On the other hand, an intrinsic parameter, such as the mean rare earth cation radius, selected through synthesis of solid solutions may be more appropriate.[14]

Solid solutions of $LaNiO_3$, the only metallic and paramagnetic $RNiO_3$ at all temperatures, with another $RNiO_3$ compound are particularly interesting. Such a phase diagram, $R_{1-x}La_xNiO_3$, would cross different phases and include magnetic and electronic quantum phase transitions, which have been studied previously.[15–19]

Less well-understood, however, is how the structure and microstructure evolve in such a solid solution. Bulk $RNiO_3$ (R ≠ La) compounds crystallize in the orthorhombic Pnma symmetry in the high temperature metallic phase and $P2_1/n$ in their low temperature insulating state.[20,21] In terms of NiO_6 octahedra, this structure can be written as $a^-b^+a^-$ in Glazer notation, meaning that the octahedra rotate in alternate directions along the a and c axes, while they all rotate in the same direction along the b axis.[3] Meanwhile, bulk $LaNiO_3$ crystallizes in the higher symmetry $R\bar{3}c$ (rhombohedral) structure at all temperatures with antiphase octahedral rotations along all crystallographic axes, in other words $a^-a^-a^-$ in Glazer notation. According to group theoretical analysis, there is no group–subgroup relation either between Pnma and $R\bar{3}c$ or between $P2_1/n$ and $R\bar{3}c$ symmetries, meaning that a continuous displacive phase transition between the structure of $LaNiO_3$ and the other $RNiO_3$ compounds is not possible.[4] The more general term "crossover" will be employed instead, and the question of how a solid solution $R_{1-x}La_xNiO_3$ will make the crossover between the two end compound symmetries, especially with an additional physical constraint, such as strain, is raised. This investigation addresses this question by combining $NdNiO_3$ and $LaNiO_3$ in solid solution thin films of $Nd_{1-x}La_xNiO_3$ epitaxially grown on two distinct substrates that impose either tensile or compressive strain.

One possibility is that the samples will be comprised of intermixed Pnma (or, at low temperature, $P2_1/n$) and $R\bar{3}c$ regions. Another possibility is that of an intermediate phase that bridges the two end compound symmetries, as was reported in the solid solution $PbZr_{1-x}Ti_xO_3$.[22] The transition from $a^-a^-a^-$ to $a^-b^+a^-$ has, in particular, been studied in $BiFeO_3$ where it was suggested that it proceeds via intermediate complex octahedral tilt patterns and unusually large unit cells of low symmetry.[23] In $Nd_{1-x}La_xNiO_3$, in principle, both higher (Imma) and lower ($P2_1/n$ or $P\bar{1}$) symmetry intermediate stages are possible. Alternatively, it may be that no bridge phase will be observed as is the case for the classical Pnma–$R\bar{3}c$ transition in polycrystalline $LaCrO_3$.[24]

How the crossover proceeds with only chemical tuning in biaxially strained films, where, in addition, biaxial strain may lower the symmetry, remains to be established. $LaNiO_3$ is reduced from $R\bar{3}c$ to C2/c ($a^-a^-a^-$ to $a^-a^-c^-$) and $NdNiO_3$ may be reduced from Pnma to possibly $P2_1/m$ or Cmcm ($a^-b^+a^-$ to $a^-b^+c^-$ or $a^0b^+c^-$).[25–27] Here, Raman spectroscopy and scanning transmission electron microscopy are combined to determine the symmetry at distinct length scales and unveil the mechanism of the crossover in $Nd_{1-x}La_xNiO_3$.

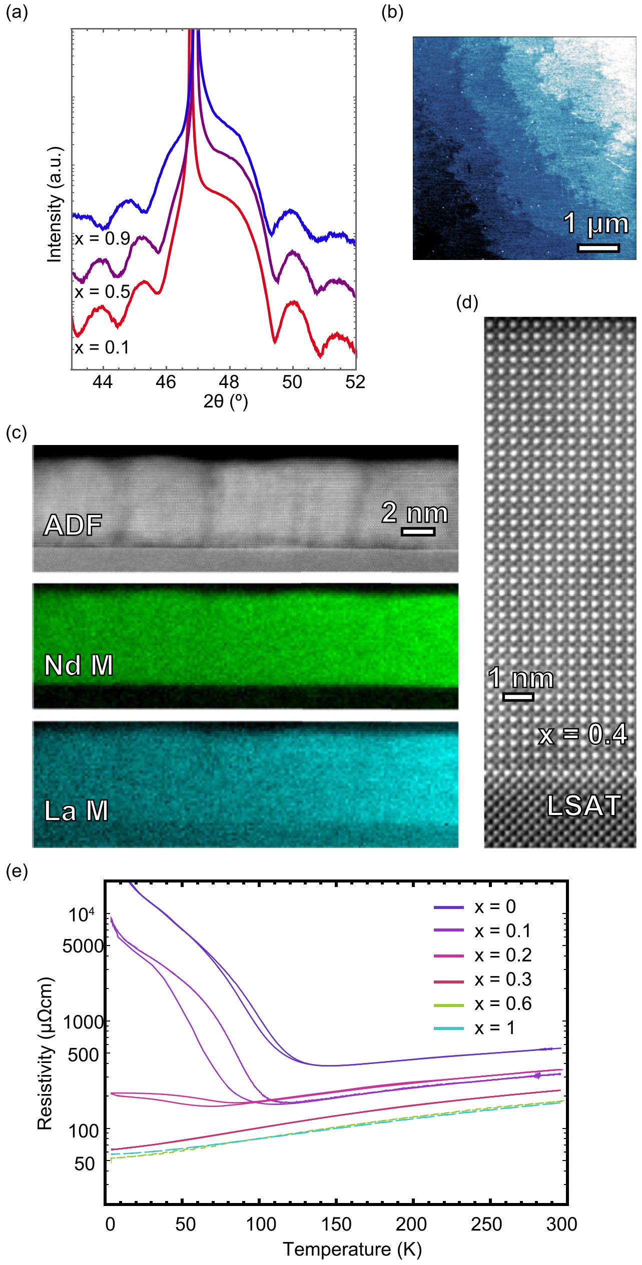

FIG. 1. (a) Finite thickness fringes around the (002) Bragg peak of 20 pseudocubic unit cell (u.c.) (8 nm) thick $Nd_{1-x}La_xNiO_3$ films grown on the LSAT substrate with $x = 0.1$, 0.5, and 0.9. (b) Tapping mode atomic force microscopy topography of 60 u.c. (23 nm) thick $Nd_{1-x}La_xNiO_3$ on the $LaAlO_3$ substrate with $x = 0.5$, revealing atomically flat terraces related to the miscut angle of the substrate. Over the image (5 × 5 μm^2), the rms roughness is 3.85 Å or ∼1 u.c. (c) Scanning transmission electron microscopy (STEM) annular dark-field (ADF) image from where the Nd (middle) and La (bottom) energy loss spectroscopy compositional maps have been obtained on a 16 u.c. (6 nm) thick $Nd_{1-x}La_xNiO_3$ film with $x = 0.25$. The Nd and La signals have been extracted from their characteristic M edges. (d) A high-angle annular dark-field (HAADF) image from scanning transmission electron microscopy (STEM) on a 40 u.c. (15 nm) film of $Nd_{1-x}La_xNiO_3$ on the LSAT substrate with $x = 0.4$. (e) Resistivity as a function of temperature for 20 u.c. (8 nm) thick $Nd_{1-x}La_xNiO_3$ films on LSAT for $x = 0$, 0.1, 0.2, 0.3, 0.6, and 1.

II. SAMPLE CHARACTERIZATION

The $Nd_{1-x}La_xNiO_3$ samples are grown as epitaxial thin films by alternate sputtering as described in Sec. VII. The high crystallinity of the resulting films is evidenced by x-ray diffraction and scanning transmission electron microscopy [Figs. 1(a) and 1(d)]. The films are found to have atomically flat step-terraced surfaces, as shown by atomic force microscopy [Fig. 1(b)]. According to electron energy loss spectroscopy—a local probe of the elemental composition—the resulting $Nd_{1-x}La_xNiO_3$ thin films are chemically homogeneous with an even distribution of Nd and La signals, as shown in Fig. 1(c). A series of various thicknesses, totaling dozens of samples, have been grown on two substrates: $(LaAlO_3)_{0.3}(Sr_2TaAlO_6)_{0.7}$ (LSAT) and $LaAlO_3$, both terminated on the (001) pseudocubic plane. LSAT and $LaAlO_3$ provide a biaxial strain of 0.8% and −1.3% to $LaNiO_3$ and 1.6% and −0.5% to $NdNiO_3$, respectively.

In going from $NdNiO_3$ to $LaNiO_3$, an insulator–metal quantum phase transition is expected at 0 K. $NdNiO_3$ has an insulator–metal transition at a temperature, T_{MI}. In bulk $NdNiO_3$, T_{MI} is around 200 K but can be lower in thin films.[12] $LaNiO_3$, on the other hand, is metallic down to the lowest temperatures but does eventually become insulating when the surface effects begin to dominate in the ultrathin regime—at thicknesses much lower than that of the films studied herein.[28–31] Figure 1(e) illustrates the transport behavior for a $Nd_{1-x}La_xNiO_3$ series of 20 pseudocubic unit cell (u.c.) (8 nm) thickness on LSAT. For $x = 0$, $T_{MI} = 120$ K; for $x = 0.2$, $T_{MI} = 80$ K; and over the temperature range investigated, the films with higher La content are all metallic with comparable resistivity as x increases. The system at low temperature, therefore, goes from insulating to metallic between $x = 0.2$ and $x = 0.3$. This is in line with the renormalization of the phase diagram by biaxial strain as previously observed.[17] The series on $LaAlO_3$ is found to be metallic for all x, similar to what has been reported in some previous works[32] and likely stemming from slight off-stoichiometry.[33]

As $Nd_{1-x}La_xNiO_3$ is metallic for all x at room temperature, a symmetry crossover from Pnma to $R\bar{3}c$ can be studied without potential electronic effects, which are only relevant at lower temperatures. The only variations with x expected at room temperature are structural.

III. RAMAN SPECTROSCOPY

In order to probe the macroscopic symmetry, Raman spectra were recorded for various compositions of $Nd_{1-x}La_xNiO_3$ on both $LaAlO_3$ and LSAT substrates as described in Sec. VII. Figures 2(a) and 2(b) show the Raman spectra for a series of 20 u.c. (8 nm) $Nd_{1-x}La_xNiO_3$ films. In the spectrum for $NdNiO_3$, three film modes are identified.[34,35] These three modes are then traced as a function of composition in Figs. 2(c) and 2(d), and the corresponding structural distortion is sketched alongside. The modes of interest are the E_g- and A_{1g}-like soft modes, where the labeling is in analogy to the bulk material. This notation is for simplicity only as the biaxial strain on the thin film reduces the symmetry in the case of $LaNiO_3$ from $R\bar{3}c$ to C2/c[25,36,37] and in the case of $NdNiO_3$ possibly from Pnma to $P2_1/m$ or Cmcm.[26,27]

For the series on both substrates, the trends are remarkably similar. The E_g-like mode denoted by the green circles is seen to gradually decrease in frequency as x increases. This mode relates to the bending of the oxygen octahedral cage, and its softening toward $LaNiO_3$ is likely to be representative of the gradual increase in bond length.[38]

The A_g-like mode shown by the red squares decreases in the wavenumber more significantly as the phase diagram is traversed.

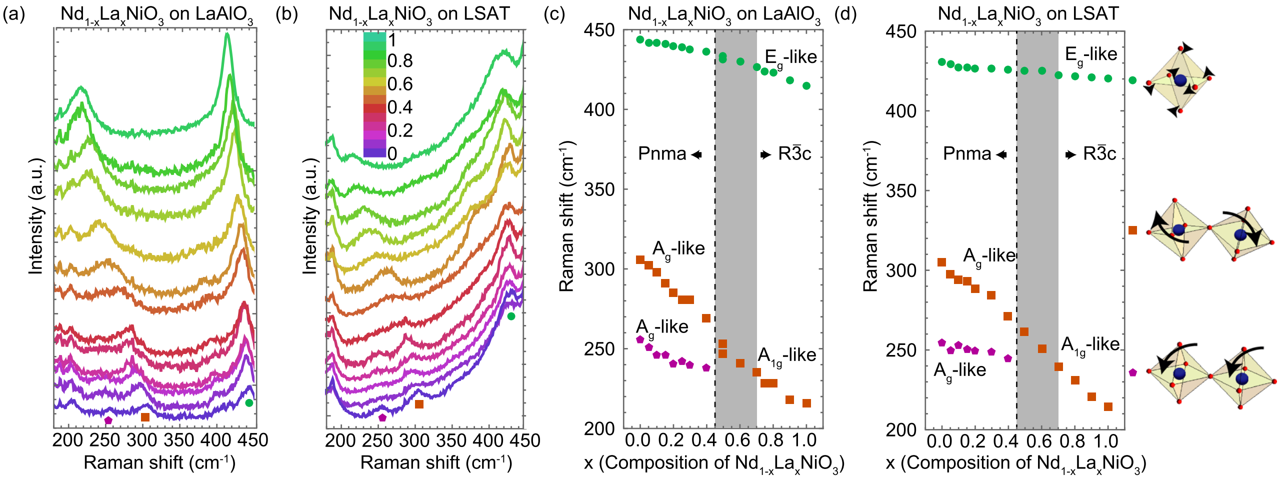

FIG. 2. (a) and (b) Room temperature Raman spectra of different compositions of $Nd_{1-x}La_xNiO_3$ of 20 u.c. (8 nm) thickness on the $LaAlO_3$ substrate and on the LSAT substrate, respectively, in the frequency range of interest. Three film modes are identified on the $x = 0$ spectrum. Spectra are shifted vertically in proportion to the composition. [(c) and (d)] Compositional dependence of the series on the $LaAlO_3$ and LSAT substrates, respectively. The Raman shifts plotted are of the three assigned modes from (a) and (b). Shown are the E_g-like modes (green circles) and the two A_{1g}-like modes corresponding to out-of-phase and in-phase octahedral rotations (red squares and purple pentagons, respectively). On the right are sketches of the relevant structural distortions. Identified phase boundaries are marked with a dashed line, and the gray box represents the region of phase coexistence discussed later.

As sketched, this mode has a vibrational pattern that corresponds to antiphase rotations of the corner-connected oxygen octahedra, known as one of the A_g "tilt modes" of Pnma perovskites.[39–41] This Pnma A_g mode is a direct counter-part of the A_{1g} mode in the $R\bar{3}c$ symmetry, as also seen in the $LaCrO_3$ case.[24] As expected, this mode also softens when crossing from $NdNiO_3$ to $LaNiO_3$ due to the corresponding decrease in the octahedral rotation angle. The linear relationship between this soft mode frequency and the rotation angle has previously been established in several perovskite systems,[39,41] where $RNiO_3$ compounds show a slope of 26.2 cm^{-1} per degree of rotation.[40]

The lower energy phonon mode plotted in Figs. 2(c) and 2(d) is shown by the purple pentagons and is also of A_g-like symmetry.[34,35] In this case, however, the structural distortion corresponds to in-phase rotations of octahedra. Similar to the other rotational mode, this one also softens with increasing La content, but it can only be followed up until a composition of $x = 0.4$. This mode is not Raman active in an $R\bar{3}c$ tilted perovskite, with its single octahedral rotation angle ($a^-a^-a^-$), and should therefore be unique to the Pnma ($a^-b^+a^-$) side of the phase diagram. It is deduced, therefore, that the disappearance of this Raman mode corresponds to a structural change from the Pnma space group. The phase boundary can therefore be sketched as a dashed line at around $x = 0.45 \pm 0.05$, agreeing well with x-ray diffraction studies on powder samples of $Nd_{1-x}La_xNiO_3$.[15] The gray shading represents a region of extended phase coexistence, as determined from STEM and discussed later.

Interestingly, the crossover composition is independent of the strain state, with LSAT providing a tensile strain and $LaAlO_3$ providing a compressive strain. Moreover, LSAT is cubic and $LaAlO_3$ is rhombohedral, so the substrate symmetry also does not seem to affect the composition of the symmetry crossover.

Regarding the mechanism of the crossover, Raman spectroscopy does not suggest an intermediate symmetry phase of either higher or lower symmetry, at least down to the resolution of composition of ±0.05.

If there are intermixed regions of distinct symmetry, however, it is possible that Raman spectroscopy would not be able to resolve them as the Raman peaks common to both symmetries would be

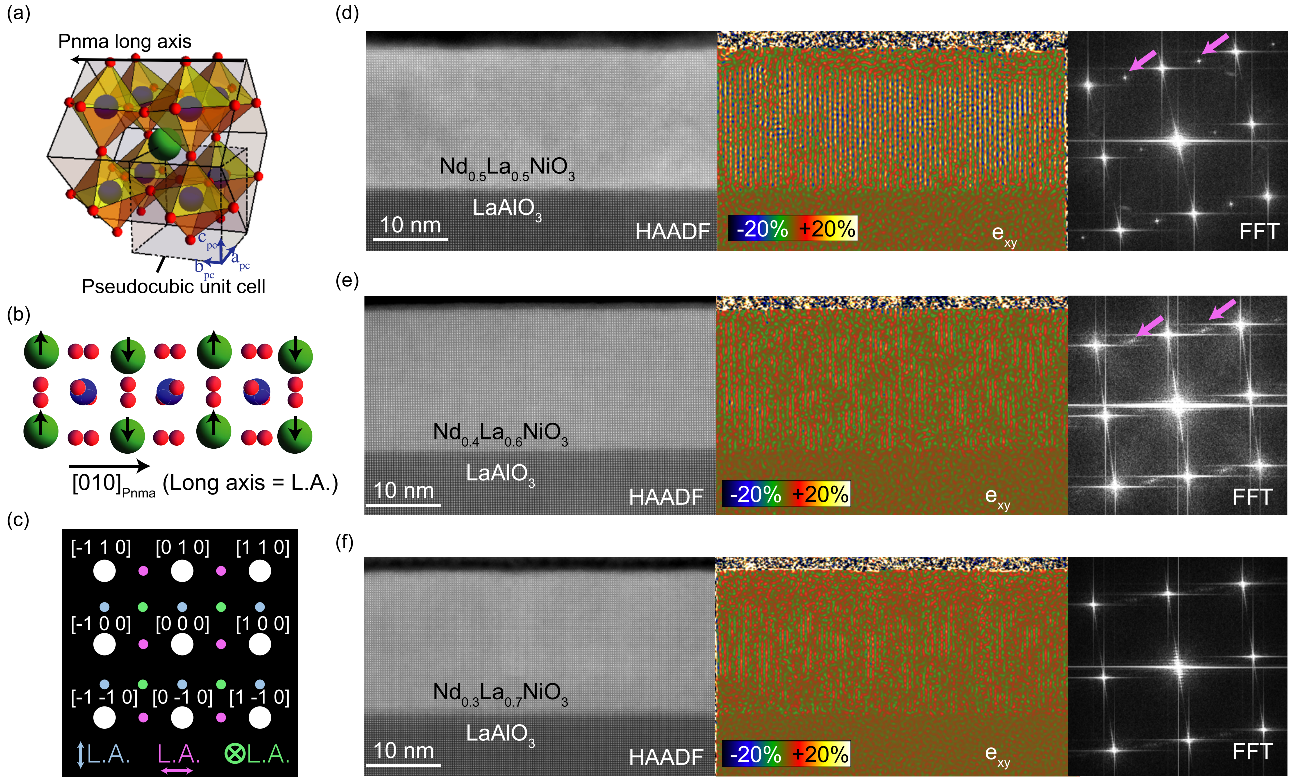

FIG. 3. (a) Pnma unit cell with respect to the pseudocubic unit cell showing that one axis, the b axis in this case, is approximately $\sqrt{2}$ longer than the other two. (b) A cut of the Pnma structure illustrating the antipolar motion occurring on the rare earth sites resulting in the shift of entire atomic columns alternately up and down. (c) A schematic of the expected Fourier transform of an orthorhombic crystal with the intensities arising from the cation anti-polar motion symmetry identified. The magenta, blue, and green spots indicate the half-order intensities generated from the Pnma long axis being oriented horizontally, vertically, and along the zone axis (normal to the image plane), respectively. [(d)–(g)] Analysis of three 65 u.c. (~25 nm) thick films of $Nd_{1-x}La_xNiO_3$ on the $LaAlO_3$ substrate with $x = 0.5$, 0.6, and 0.7, respectively. The first column shows a high-angle annular dark-field (HAADF) image, the central column shows the corresponding GPA e_{xy} component map, and the rightmost column shows the corresponding fast Fourier transform (FFT) pattern. In the FFT patterns, which were obtained from slightly rotated images, half-order intensities arising from the Pnma long axis lying in the plane of the film are clearly seen for $x = 0.5$ and $x = 0.6$. The ($\frac{1}{2}$, 1, 0) and ($-\frac{1}{2}$, 1, 0) pseudocubic reflections are indicated by arrows as examples. The color scale of the GPA maps indicates the shear deformation amplitude associated with the cations with respect to the pseudocubic unit cell size of the $LaAlO_3$ substrate.

very close in frequency since the chemical composition is the same. In addition, depending on the scale of the co-existing regions of distinct symmetry, it may be that the phonon modes become poorly defined.

IV. STEM

As a complement to the Raman spectroscopy, which provides information on the macroscopic symmetries, the atomic-scale lattice structure can be analyzed by scanning transmission electron microscopy (STEM).

Raman spectra show that $NdNiO_3$ and $Nd_{1-x}La_xNiO_3$ up to at least $x = 0.4$ are orthorhombic at room temperature with the space group Pnma. A sketch of the unit cell and its relationship to the pseudocubic unit cell is shown in Fig. 3(a). Within this crystal symmetry, the A-site cations (here, the rare earths) cooperatively displace in an antipolar motion, as schematized in Fig. 3(b). Looking for this antipolar motion not only allows the rhombohedral and orthorhombic structures to be distinguished but also the direction of the orthorhombic long axis [the b axis in Fig. 3(a)] to be determined. These displacements, however, are on the order of picometers, so detecting them by image inspection alone may be challenging. This necessitates alternative analytical approaches.

The pseudocubic unit cell doubling resulting from the A-site displacements generates additional reflections at half-order positions in the fast Fourier transform (FFT) patterns of the high-angle annular dark-field (HAADF) images. Figure 3(c) sketches an example FFT where the reflections arising from the Pnma long axis (LA) lying horizontally, vertically, and along the zone axis are indicated by magenta, blue, and green spots, respectively. The structural symmetries at the nanometric scale can be analyzed by using the geometric phase analysis (GPA) plug-in for digital micrograph. Conventionally, GPA is used to determine the strain fields of a lattice image.[42] This involves centering two apertures at two lattice reflections in the FFT of the image and then performing the inverse Fourier transform. Here, by first centering the apertures on the first-order pseudocubic unit cell reflections and then increasing their reciprocal space size to include the half-order reflections, parallel fringes appear in both the shear (e_{xy}) and rotation (r_{xy}) strain maps. The nature of these fringes relates to the shear deformation and cell rotation that each pseudocubic unit cell undergoes due to the rippling pattern of the rare earth cation antipolar displacements, with alternating signs along the orthorhombic long axis.[43]

Figures 3(d)–3(f) show the HAADF images (left column), GPA e_{xy} strain maps (central column), and FFT patterns (right column) obtained from 65 u.c. (25 nm) $Nd_{1-x}La_xNiO_3$ thin films grown on $LaAlO_3$ with compositions $x = 0.5$, 0.6, and 0.7.

The fringes that clearly appear in the GPA e_{xy} strain maps of the first two samples allow the film symmetries to be identified as Pnma. This is an apparent contradiction to the Raman spectroscopy where the relevant phonon mode was only observed up to $x = 0.4$.

The fringes are aligned vertically, parallel to the surface normal. This indicates that the Pnma long axis lies in the plane of the film. This is expected for a compressively strained system as the Pnma long axis is slightly shorter than the hypotenuse across the other two Pnma axes. Here, note that geometrically equivalent domains of the film with the Pnma long axis parallel to the zone axis are observed in other regions, as identified by the additional reflections in the FFT pattern, but do not give rise to fringes in the GPA e_{xy} strain maps. As the lanthanum content is increased, the fringes, although still visible, become less striking, while the color scale shows that the amplitude of the antipolar motion is decreased. For $x = 0.6$, and especially for $x = 0.7$, although faint fringes are still observed, there are

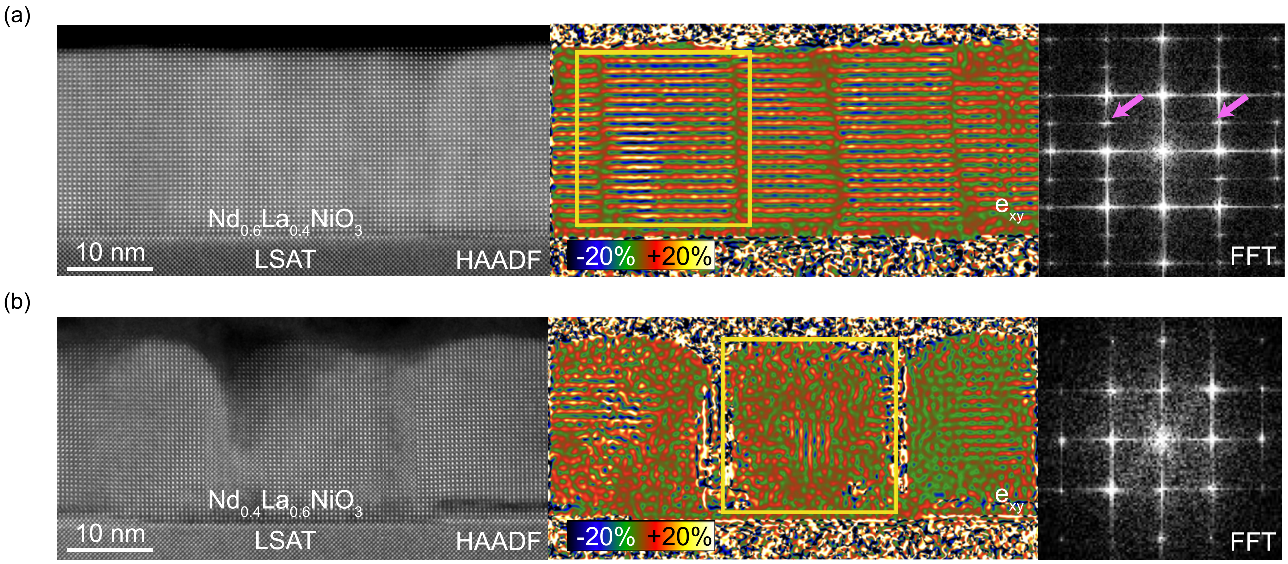

FIG. 4. HAADF images, the associated GPA e_{xy} component maps, and fast Fourier transform patterns acquired from 40 u.c. (15 nm) thick $Nd_{1-x}La_xNiO_3$ on LSAT with $x = 0.4$ and 0.6 in (a) and (b), respectively. The FFT patterns are generated from the region highlighted by the yellow square in the GPA maps. The color scale bar indicates the antipolar shift of the cations as a percentage of the pseudocubic unit cell size. The $(1, \frac{1}{2}, 0)$ and $(-1, \frac{1}{2}, 0)$ reflections are indicated on the FFT pattern by magenta arrows.

significant portions of the film that lack long-range cation ordering. At these compositions, the Raman spectra exhibit the peaks expected for pure $LaNiO_3$, so these non-cation-ordered regions are deduced to be rhombohedral-like in symmetry. The rhombohedral regions seem to preferentially exist close to the interface with the substrate and at the surface. The $x = 0.5$ film, despite its clear fringes, also exhibits a few nm thick non-Pnma region at the interface and, to a lesser extent, at the surface.

The final column shows the FFT patterns of the HAADF images in column (i). The half-order intensities expected to arise from an in-plane Pnma long axis are clearly observed for $x = 0.5$, as shown by the magenta arrows. At $x = 0.6$, the half-order diffraction spots are still detected but have become elongated and slightly diffuse, indicating a lack of long-range order due to the reduction in the Pnma-ordered volume. For the $x = 0.7$ film, only very faint half-order intensity is observed and the FFT pattern largely corresponds to what would be expected for a purely rhombohedral structure.

These results show that for $Nd_{1-x}La_xNiO_3$ on the $LaAlO_3$ substrate, there is a range of compositions where Pnma and $R\bar{3}c$ symmetries coexist with the higher symmetry rhombohedral phase growing inward from the interface and the surface.

Figure 4 illustrates an analogous study for the series of $Nd_{1-x}La_xNiO_3$ on LSAT. Here, the picture is a little more complex and the presence of Ruddlesden–Popper (RP) stacking faults renders the analysis and interpretation slightly more challenging.

Figure 4(a) shows the HAADF image, GPA e_{xy} map, and FFT pattern for a sample of $Nd_{1-x}La_xNiO_3$ with x = 0.4 on LSAT. The fringes due to the antipolar motion are observed, confirming that this sample is of Pnma symmetry. Additional half-order reflections in the FFT support this. Contrary to the compressive strain imposed by the $LaAlO_3$ substrate, the biaxial strain is now tensile and, consequently, the Pnma long axis is observed to be oriented normal to the film surface.

On the other hand, Fig. 4(b), for $x = 0.6$, does not show clear fringes due to the antipolar motion, but there is some suggestion of ordering in very small regions, similar to the $x = 0.7$ sample on $LaAlO_3$. Here, however, the non-Pnma regions appear to align more closely with the vertical RP stacking faults evident in the HAADF. The insets of Fig. 4 are the FFT of the region indicated by the yellow square, and no half-order reflections are observed, confirming the result from Raman spectroscopy that, overall, this sample is not of Pnma symmetry but rather the higher symmetry $R\bar{3}c$, albeit reduced to C2/c by the biaxial strain.

V. DISCUSSION

With regard to the $Nd_{1-x}La_xNiO_3$ symmetry crossover, Raman spectroscopy can follow the Pnma symmetry up to $x = 0.4$ irrespective of the strain state provided by the substrate. The GPA maps from STEM, however, reveal that up to around $x = 0.6$, significant portions of the film retain Pnma symmetry. The short scale of these Pnma-ordered regions of a few nm is also evidenced by the elongated and diffuse nature of the half-order reflections in the FFT pattern. The confined Pnma volume when there is phase coexistence is likely the reason that this symmetry is no longer detected by Raman spectroscopy. While the compositional range at which $Nd_{1-x}La_xNiO_3$ hosts the two symmetries is similar for both tensile strain and compressive strain, the nature of this intermixed state is quite distinct. On LSAT, the $R\bar{3}c$ phase stabilizes more readily close to defects, such as RP stacking faults, while on $LaAlO_3$, the rhombohedral phase evolves inward from the surface and the interface upon increasing x. These distinct mechanisms may come from the sign of the strain state or substrate symmetry. What may also play a role is the difference in quality, with tensile strain resulting in more defects in the $Nd_{1-x}La_xNiO_3$ films and therefore promoting nucleation of the higher symmetry phase along fault lines rather than at the boundaries of the thin film.

Both Raman spectroscopy and STEM analyses indicate that there is no significant intermediate phase of symmetry distinct from either Pnma or $R\bar{3}c$ in the biaxially strained $Nd_{1-x}La_xNiO_3$ system.

It is possible that the physical properties of the $Nd_{1-x}La_xNiO_3$ films, for instance conductivity, could be influenced by the symmetry crossover—through modifications of the bandwidth—and the phase coexistence—through increased scattering from the boundaries.

VI. CONCLUSIONS

Through combining the complementary techniques of Raman spectroscopy and STEM, the room temperature Pnma-$R\bar{3}c$ crossover in solid solution thin films of $Nd_{1-x}La_xNiO_3$ has been analyzed.

Raman spectroscopy provides a powerful and efficient tool to study the symmetries and phase transitions in solid state systems. On the other hand, STEM reveals a very local, atomic-scale picture of a complex evolution of the phase coexistence.

The crossover from Pnma is seen to start at around $x = 0.5$ at room temperature with regions of phase coexistence with both Pnma and $R\bar{3}c$ symmetries until around $x = 0.7$, regardless of the sign of the biaxial strain or the substrate symmetry.

These observations confirm what was expected for the consideration of these two space groups and show that solid solutions of the type $R_{1-x}La_xNiO_3$ do not represent a continuous tuning in terms of the lattice. Instead of an intermediate symmetry phase, the system preferentially allows the distinct symmetries to coexist, while the evolution of the two phases with composition depends strongly on the substrate used. What is clear, then, is that this region of the rare earth nickelate phase diagram is not tunable in an analog fashion through synthesis of solid solutions, knowledge that may prove to be important in the quest for materials-by-design.

VII. METHODS

A. Sample preparation

The $Nd_{1-x}La_xNiO_3$ films were grown by radio-frequency off-axis magnetron sputtering at a temperature of 450 °C, in an $Ar:O_2$ ratio of 7:2 and a pressure of 0.18 Torr. The solid solution was achieved by intermittently sputtering from two stoichiometric ceramic targets of $NdNiO_3$ and $LaNiO_3$. The individual growth rates of the two end compounds were calculated by fitting finite thickness fringes in x-ray diffraction,[44] and these rates were then used to determine the length of time of intermittent sputtering to achieve the desired composition. The intermittent growth is set so that after each repeat of sputtering from $NdNiO_3$ and $LaNiO_3$, a total of 40% of a unit cell has been deposited. Energy dispersive x-ray spectroscopy performed in the electron microscope shows that the Nd:La ratio is in agreement with the nominal x within the experimental error.

B. Raman spectroscopy

Raman spectroscopy measurements were performed using an InVia Renishaw micro-Raman spectrometer with a 633 nm He–Ne laser line.

C. STEM

The STEM samples were prepared by mechanical tripod polishing followed by argon ion beam milling until electron transparency. Stacks of high-angle annular dark-field (HAADF) images were acquired in a double-aberration-corrected FEI (Thermo Fisher Scientific) Titan Themis 60-300 microscope located at the Interdisciplinary Centre for Electron Microscopy (CIME), École Polytechnique Fédérale de Lausanne (EPFL). The microscope was operated at 300 kV with a convergence semi-angle of 20 mrad. The images of each stack are aligned with the SmartAlign plug-in for Digital Micrograph (GMS3.2), which corrects the image drift and the linear and non-linear scan distortions.[45]

STEM-EELS spectrum image datasets were acquired with a Gatan GIF Quantum ERS spectrometer using the following conditions: a collection semiangle of ≈47 mrad, 0.01 s acquisition time per pixel, and an energy dispersion of 0.5 eV/channel. EEL spectra were denoised by principal component analysis.

D. Transport

The $Nd_{1-x}La_xNiO_3$ films were etched into a Hall bar and then contacted by Al bonds onto sputtered Pt pads. The transport measurements were recorded in a ^{4}He dipping station.

ACKNOWLEDGMENTS

This work was supported by the Swiss National Science Foundation through Division II, Project No. 200020_179155. Marta Gibert acknowledges support by the Swiss National Science Foundation under Grant No. PP00P2_170564. The research leading to these results had received funding from the European Research Council under the European Union's Seventh Framework Program (FP7/2007-2013)/ERC, Grant Agreement No. 319286 (Q-MAC). A.S., C.T., Mael Guennou, and J.K. acknowledge support from the Luxembourg National Research Fund under Project No. CO-FERMAT FNR/P12/4853155/Kreisel and the AFR, Grant No. 7749159.

DATA AVAILABILITY

The data that support the findings of this study is available at https://doi.org/10.26037/yareta:oonzm7k6kfcajgiihcffkxjhci.

REFERENCES

[1] R. H. Mitchell, *Perovskites: Modern and Ancient* (Almaz, 2003).

[2] J. B. Goodenough, "Electronic and ionic transport properties and other physical aspects of perovskites," Rep. Prog. Phys. **67**, 1915–1993 (2004).

[3] A. M. Glazer, "Simple ways of determining perovskite structures," Acta Crystallogr., Sect. A: Found. Adv. **31**, 756 (1975).

[4] C. J. Howard and H. T. Stokes, "Group-theoretical analysis of octahedral tilting in perovskites," Acta Crystallogr., Sect. B: Struct. Sci., Cryst. Eng. Mater. **54**, 782–789 (1998).

[5] C. J. Howard and H. T. Stokes, "Structures and phase transitions in perovskites—A group-theoretical approach," Acta Crystallogr., Sect. A: Found. Adv. **61**, 93–111 (2005).

[6] C. J. Howard and M. A. Carpenter, "Octahedral tilting in cation-ordered Jahn–Teller distorted perovskites—A group-theoretical analysis," Acta Crystallogr., Sect. B: Struct. Sci., Cryst. Eng. Mater. **66**, 40–50 (2010).

[7] M. A. Carpenter and C. J. Howard, "Symmetry rules and strain/order-parameter relationships for coupling between octahedral tilting and cooperative Jahn–Teller transitions in ABX_3 perovskites. I. Theory," Acta Crystallogr., Sect. B: Struct. Sci., Cryst. Eng. Mater. **65**, 134–146 (2009).

[8] J. A. Alonso, J. L. García-Muñoz, M. T. Fernández-Díaz, M. A. G. Aranda, M. J. Martínez-Lope, and M. T. Casais, "Charge disproportionation in $RNiO_3$ perovskites: Simultaneous metal-insulator and structural transition in $YNiO_3$," Phys. Rev. Lett. **82**, 3871–3874 (1999).

[9] A. Mercy, J. Bieder, J. Íñiguez, and P. Ghosez, "Structurally triggered metal-insulator transition in rare-earth nickelates," Nat. Commun. **8**, 1677 (2017).

[10] M. L. Medarde, "Structural, magnetic and electronic properties of $RNiO_3$ perovskites (R = rare earth)," J. Phys.: Condens. Matter **9**, 1679–1707 (1997).

[11] G. Catalan, "Progress in perovskite nickelate research," Phase Transitions **81**, 729–749 (2008).

[12] S. Catalano, M. Gibert, J. Fowlie, J. Íñiguez, J.-M. Triscone, and J. Kreisel, "Rare-earth nickelates $RNiO_3$: Thin films and heterostructures," Rep. Prog. Phys. **81**, 046501 (2018).

[13] P. C. Canfield, J. D. Thompson, S.-W. Cheong, and L. W. Rupp, "Extraordinary pressure dependence of the metal-to-insulator transition in the charge-transfer compounds $NdNiO_3$ and $PrNiO_3$," Phys. Rev. B **47**, 12357–12360 (1993).

[14] C. Girardot, J. Kreisel, S. Pignard, N. Caillault, and F. Weiss, "Raman scattering investigation across the magnetic and metal-insulator transition in rare earth nickelate $RNiO_3$ (R = Sm, Nd) thin films," Phys. Rev. B **78**, 104101 (2008).

[15] J. Blasco and J. Garcia, "Structure, magnetic and electrical properties in $Nd_{1-x}La_xNiO_3$ system," Solid State Ionics **63-65**, 593–598 (1993).

[16] J. Blasco and J. Garcia, "A comparative study of the crystallographic, magnetic and electrical properties of the $Nd_{1\text{-x}}La_xNiO_{3\text{-delta}}$ system," J. Phys.: Condens. Matter **6**, 10759–10772 (1994).

[17] A. S. Disa, D. P. Kumah, J. H. Ngai, E. D. Specht, D. A. Arena, F. J. Walker, and C. H. Ahn, "Phase diagram of compressively strained nickelate thin films," APL Mater. **1**, 032110 (2013).

[18] B. A. Frandsen, L. Liu, S. C. Cheung, Z. Guguchia, R. Khasanov, E. Morenzoni, T. J. Munsie, A. M. Hallas, M. N. Wilson, Y. Cai, G. M. Luke, B. Chen, W. Li, C. Jin, C. Ding, S. Guo, F. Ning, T. U. Ito, W. Higemoto, S. J. Billinge, S. Sakamoto, A. Fujimori, T. Murakami, H. Kageyama, J. A. Alonso, G. Kotliar, M. Imada, and Y. J. Uemura, "Volume-wise destruction of the antiferromagnetic Mott insulating state through quantum tuning," Nat. Commun. **7**, 12519 (2016).

[19] D. J. Gawryluk, Y. M. Klein, T. Shang, D. Sheptyakov, L. Keller, N. Casati, P. Lacorre, M. T. Fernández-Diáz, J. Rodríguez-Carvajal, and M. Medarde, "Distortion mode anomalies in bulk $PrNiO_3$: Illustrating the potential of symmetry-adapted distortion mode analysis for the study of phase transitions," Phys. Rev. B **100**, 205137 (2019).

[20] J. L. García-Muñoz, J. Rodríguez-Carvajal, P. Lacorre, and J. B. Torrance, "Neutron-diffraction study of $RNiO_3$ (R = La, Pr, Nd, Sm): Electronically induced structural changes across the metal-insulator transition," Phys. Rev. B **46**, 4414–4425 (1992).

[21] J. A. Alonso, M. J. Martínez-Lope, M. T. Casais, M. A. G. Aranda, and M. T. Fernández-Díaz, "Metal–insulator transitions, structural and microstructural evolution of $RNiO_3$ (R = Sm, Eu, Gd, Dy, Ho, Y) perovskites: Evidence for room-temperature charge disproportionation in monoclinic $HoNiO_3$ and $YNiO_3$," J. Am. Chem. Soc. **121**, 4754–4762 (1999).

[22] B. Noheda, D. E. Cox, G. Shirane, J. A. Gonzalo, L. E. Cross, and S.-E. Park, "A monoclinic ferroelectric phase in the $Pb(Zr_{1-x}Ti_x)O_3$ solid solution," Appl. Phys. Lett. **74**, 2059 (1999); arXiv:9903007 [cond-mat].

[23] S. Prosandeev, D. Wang, W. Ren, J. Íñiguez, and L. Bellaiche, "Novel nanoscale twinned phases in perovskite oxides," Adv. Funct. Mater. **23**, 234–240 (2013).

[24] M. N. Iliev, A. P. Litvinchuk, V. G. Hadjiev, Y. Q. Wang, J. Cmaidalka, R. L. Meng, Y. Y. Sun, N. Kolev, and M. V. Abrashev, "Raman spectroscopy of low-temperature (*Pnma*) and high-temperature ($R\bar{3}c$) phases of $LaCrO_3$," Phys. Rev. B **74**, 214301 (2006).

[25] M. C. Weber, M. Guennou, N. Dix, D. Pesquera, F. Sánchez, G. Herranz, J. Fontcuberta, L. López-Conesa, S. Estradé, F. Peiró, J. Iñiguez, and J. Kreisel, "Multiple strain-induced phase transitions in $LaNiO_3$ thin films," Phys. Rev. B **94**, 014118 (2016).

[26] J. Y. Zhang, H. Kim, E. Mikheev, A. J. Hauser, and S. Stemmer, "Key role of lattice symmetry in the metal-insulator transition of $NdNiO_3$ films," Sci. Rep. **6**, 23652 (2016).

[27] A. Vailionis, H. Boschker, W. Siemons, E. P. Houwman, D. H. A. Blank, G. Rijnders, and G. Koster, "Misfit strain accommodation in epitaxial ABO_3 perovskites: Lattice rotations and lattice modulations," Phys. Rev. B **83**, 064101 (2011).

[28] J. Son, P. Moetakef, J. M. Lebeau, D. Ouellette, L. Balents, S. J. Allen, and S. Stemmer, "Low-dimensional Mott material: Transport in ultrathin epitaxial $LaNiO_3$ films," Appl. Phys. Lett. **96**, 062114 (2010).

[29] R. Scherwitzl, S. Gariglio, M. Gabay, P. Zubko, M. Gibert, and J. M. Triscone, "Metal-insulator transition in ultrathin $LaNiO_3$ films," Phys. Rev. Lett. **106**, 246403 (2011).

[30] J. Fowlie, M. Gibert, G. Tieri, A. Gloter, J. Íñiguez, A. Filippetti, S. Catalano, S. Gariglio, A. Schober, M. Guennou, J. Kreisel, O. Stéphan, and J. M. Triscone, "Conductivity and local structure of $LaNiO_3$ thin films," Adv. Mater. **29**, 1605197 (2017).

[31] A. Schober, J. Fowlie, M. Guennou, M. C. Weber, H. Zhao, J. Íñiguez, M. Gibert, J.-M. Triscone, and J. Kreisel, "Vibrational properties of $LaNiO_3$ films in the ultrathin regime," APL Mater. **8**, 061102 (2020).

[32] S. Middey, J. Chakhalian, P. Mahadevan, J. W. Freeland, A. J. Millis, and D. D. Sarma, "Physics of ultrathin films and heterostructures of rare-earth nickelates," Annu. Rev. Mater. Res. **46**, 305–334 (2016).

[33] D. Preziosi, A. Sander, A. Barthélémy, and M. Bibes, "Reproducibility and off-stoichiometry issues in nickelate thin films grown by pulsed laser deposition," AIP Adv. **7**, 015210 (2017).

[34] M. Zaghrioui, A. Bulou, P. Lacorre, and P. Laffez, "Electron diffraction and Raman scattering evidence of a symmetry breaking at the metal-insulator transition of $NdNiO_3$," Phys. Rev. B **64**, 081102(R) (2001).

[35] S. Prosandeev, L. Bellaiche, and J. Íñiguez, "*Ab initio* study of the factors affecting the ground state of rare-earth nickelates," Phys. Rev. B **85**, 214431 (2012).

[36] S. J. May, J. W. Kim, J. M. Rondinelli, E. Karapetrova, N. A. Spaldin, A. Bhattacharya, and P. J. Ryan, "Quantifying octahedral rotations in strained perovskite oxide films," Phys. Rev. B **82**, 014110 (2010); arXiv:1002.1317.

[37] J. Fowlie, C. Lichtensteiger, M. Gibert, H. Meley, P. Willmott, and J.-M. Triscone, "Thickness-dependent perovskite octahedral distortions at heterointerfaces," Nano Lett. **19**, 4188–4194 (2019).

[38] G. Gou, I. Grinberg, A. M. Rappe, and J. M. Rondinelli, "Lattice normal modes and electronic properties of the correlated metal $LaNiO_3$," Phys. Rev. B **84**, 144101 (2011).

[39] M. C. Weber, J. Kreisel, P. A. Thomas, M. Newton, K. Sardar, and R. I. Walton, "Phonon Raman scattering of $RCrO_3$ perovskites (R = Y, La, Pr, Sm, Gd, Dy, Ho, Yb, Lu)," Phys. Rev. B **85**, 054303 (2012).

[40] N. D. Todorov, M. V. Abrashev, and V. G. Ivanov, "Frequency dependence of the quasi-soft Raman-active modes in rotationally distorted $R^{3+}B^{3+}O_3$ perovskites (R^{3+} rare earth, B^{3+} = Al, Sc, Ti, V, Cr, Mn, Fe, Co, Ni, Ga)," J. Phys.: Condens. Matter **24**, 175404 (2012).

[41] M. C. Weber, M. Guennou, H. J. Zhao, J. Íñiguez, R. Vilarinho, A. Almeida, J. A. Moreira, and J. Kreisel, "Raman spectroscopy of rare-earth orthoferrites $RFeO_3$ (R = La, Sm, Eu, Gd, Tb, Dy)," Phys. Rev. B **94**, 214103 (2016).

[42] M. J. Hÿtch, E. Snoeck, and R. Kilaas, "Quantitative measurement of displacement and strain fields from HREM micrographs," Ultramicroscopy **74**, 131–146 (1998).

[43] H. Meley, Karandeep, L. Oberson, J. De Bruijckere, D. T. Alexander, J. M. Triscone, P. Ghosez, and S. Gariglio, "Structural analysis of $LaVO_3$ thin films under epitaxial strain," APL Mater. **6**, 046102 (2018).

[44] C. Lichtensteiger, "*InteractiveXRDFit*: A new tool to simulate and fit X-ray diffractograms of oxide thin films and heterostructures," J. Appl. Crystallogr. **51**, 1745–1751 (2018).

[45] L. Jones, H. Yang, T. J. Pennycook, M. S. Marshall, S. Van Aert, N. D. Browning, M. R. Castell, and P. D. Nellist, "Smart align—A new tool for robust non-rigid registration of scanning microscope data," Adv. Struct. Chem. Imaging **1**, 8 (2015).